Peter Griebel
First *Last*

ASME Paper Title: EVALUATION OF CURRENT AND FUTURE AVIATION FUELS AT HIGH-PRESSURE RQL-TYPE COMBUSTOR CONDITIONS

Authors: Peter Griebel, Fabian Hampp, Rainer Lückerath, Oliver Lammel, Tobias Grein, Reetu Sallinen, Jesse Vilja, Kati Sandberg

ASME Journal Title: Evaluation of Current and Future Aviation Fuels at High-pressure RQL-type Combustor Conditions

Volume/Issue 147___________________________

Date of Publication (VOR* Online) 16.10.2024_________

ASME Digital Collection URL: https://asmedigitalcollection.asme.org/gasturbinespower/article/147/4/041012/1
of-Current-and-Future-Aviation-Fuels-at

DOI: 10.1115/1.4066350

ASME Journal of Engineering for Gas Turbines and Power

EVALUATION OF CURRENT AND FUTURE AVIATION FUELS AT HIGH-PRESSURE RQL-TYPE COMBUSTOR CONDITIONS

Peter Griebel[1] **Fabian Hampp**[2] **Rainer Lückerath**[1] **Oliver Lammel**[1]

Tobias Grein[1] **Reetu Sallinen**[3] **Jesse Vilja**[3] **Kati Sandberg**[3]

[1] DLR, Institute of Combustion Technology, Stuttgart, Germany

[2] University of Stuttgart, Institute of Combustion Technology for Aerospace Engineering, Germany

[3] Neste Corporation, Technology Center, Porvoo, Finland

ABSTRACT

De-carbonizing the aviation sector is one of the biggest challenges to minimize climate change effects associated with carbon dioxide emission. Sustainable aviation fuels will play a major role in this context especially for long-distance flights where hydrogen or all-electric propulsion systems do not present a feasible alternative. In addition, aromatic-free sustainable aviation fuels offer a promising solution to lower soot emissions of aeroengines. Jet A-1 as reference fuel, 2 blends and two neat synthesized paraffinic kerosenes from hydro-processed esters and fatty acids were tested to characterize the combustion behavior of drop-in / near drop-in fuels. Experiments in an optically accessible high-pressure RQL-type combustor at typical aeroengine conditions were performed using optical diagnostics, exhaust gas and particle sampling measurements to delineate the fuel effects on spray, flame and emission characteristics. Measurements were performed at pressures up to 10 bar, air preheating temperatures up to 773 K and primary zone equivalence ratios up to 1.66. Liquid fuel distribution and fuel placement were found to be sensitive to fuel properties. By contrast, no pronounced influence on flame position and shape were observed. As a consequence, NOx and CO emissions of the tested fuels differed only moderately. However, particulate matter measurements at the fuel richest operating condition showed a clear fuel ranking with the lowest particle emissions evident for the two neat HEFA-SPK samples. Moreover, the particle volume concentration at the fuel richest condition followed the expected trend with fuel H-content.

Keywords: Sustainable aviation fuels (SAF), HEFA-SPK, combustion characteristics, high-pressure, optical access, RQL-type combustor

NOMENCLATURE

d_p	particle diameter
$EINO_x$	emission index of NO_x
EICO	emission index of CO
f	focal length
l_{pd}	penetration depth
p	pressure
P_{th}	thermal power
SMD	Sauter mean diameter
T_a	air preheating temperature
λ	wavelength
Φ_{pz}	primary zone equivalence ratio
Φ_{sz}	secondary zone equivalence ratio

1. INTRODUCTION

Sustainable aviation fuels have been identified as the primary solution to decarbonise the commercial aviation sector. Investigating the possibilities of electrification and hydrogen propulsion systems from a greenhouse gas (GHG) reduction perspective is essential. However, their wider adoption is estimated to be limited to commuter and regional operations in the electric-powered propulsion system's case and for hydrogen-powered systems up to medium haul operations. SAF on the other hand is a solution that can be deployed at needed scale and across all aircraft segments, including long haul operations that account for the majority of emitted GHG [1, 2].

The commonplace acronym SAF implies that it is made from sustainable raw material, often renewable or waste-derived, or in a broadly defined manner that the fuel is conserving an ecological balance by avoiding the depletion of natural resources [3]. To be exact, raw material or feedstock needs to meet sustainability criteria defined in established frameworks like the Carbon Offsetting and Reduction Scheme for International Aviation (CORSIA) from the International Civil Aviation Organization (ICAO) [4] or the Renewable Energy Directive of the European Union [5]. Feedstocks that meet these criteria can be refined with different processing technologies in order to create fuel components that are suitable for aviation use. To be certified for aviation use, the fuel component must be manufactured via an approved pathway defined in the standard specification for aviation turbine fuel containing synthesized hydrocarbons ASTM D7566 [6], and to meet the quality requirements set for that pathway in a respective annex of aforesaid standard. Officially, the resulting synthesized hydrocarbons meeting these requirements are called synthetic blending components (SBC). Currently the blending of SBCs is limited up to 50 vol % to conventional aviation turbine fuels typically meeting ASTM D1655 [7] or DEF-STAN 91-091 [8]. Some of the SBCs have even lower allowed limits.

One of the current commercially available pathways, and one with significant potential in terms of announced production capacity coming online and considering technology readiness level is HEFA [2]. Currently, common feedstock for the HEFA pathway is waste and residue lipids, such as used cooking oil [2]. Due to hydroprocessing the resulting hydrocarbons are paraffinic and referred to in the ASTM D7566 standard as synthesized paraffinic kerosene (SPK). The SPK's hydrocarbon composition is different from conventional aviation fuel, which can have measurable effects on the combustion performance and emissions. Paraffinic kerosene-type SAF contains almost no aromatics and has a higher hydrogen content. Due to the lack of aromatics, very low soot emissions can be achieved. The higher H-content of SPK is beneficial with respect to achieving a higher reactivity resulting in a better combustion performance. Using SPKs can also offer the potential to lower NO_x and CO emissions. However, more research is needed to elucidate the dependencies and the potential.

Considering the future target of replacing conventional Jet A-1 with SAF, it is important to investigate the fuel effects on combustion performance and emissions. The objective is to optimize both, future aeroengines and fuels in order to meet the decarbonization targets of the aviation sector. Regarding optimisation, two principal development strategies can be followed. The first, short- to mid-term one is the development of SAF that reproduces closely the combustion characteristics of Jet A-1 to facilitate the use of existing combustor hardware. The second, mid- to long-term strategy is the co-development of SAF in combination with new combustion systems. The latter approach is more promising because of a higher emission (NO_x, CO, soot) saving potential.

Differences in the chemical composition of the fuel affect emissions. Many studies report a reduction in particulate matter and soot emissions when using SAF in combustors and aeroengines [9, 10]. For example, Schripp et al. [11] investigated 49 % HEFA-SPK blends in a V2527-A5 engine and observed a reduction of non-volatile particle mass emissions up to 70 % at low power settings. Similar findings were made in the ECLIF3 campaign [12] where non-volatile particle emissions reduction of 35 % were observed at cruise conditions with a Rolls-Royce Trent XWB-84 engine while comparing 100 % HEFA-SPK to a relatively clean Jet A-1. This reduction has been linked to the reduction or absence of soot precursors such as mono-aromatic and di-aromatic/naphthalene compounds in the fuel.

Significance of the fuel composition to gaseous emissions from measurements of similar test setups as described above are not as clear as fuel composition's impact to soot propensity. According to Blakey et al. [9] some measurements show a reduction in NO_x of up to 12 % when using neat synthetic fuel but it is sometimes unclear whether this reduction can be fully attributed to the fuel composition because of uncertainties in the corrections for ambient humidity and temperature. Other studies have found no significant differences regarding NO_x [11, 13, 14]. This observation is also supported by recent results from the aforementioned ECLIF3 campaign [12] in which no measurable fuel effect on NO_x emission index was found [15]. The impact of alternative fuels on CO emissions have been investigated in [9] and depending on the engine, a change in CO emissions ranged from a reduction of up to 20 % to an increase of 8 %.

In summary, one has to be careful in comparing the reported gaseous emission reductions cited in literature because those are engine specific and also depend on the exact properties of the reference fuel used.

In this paper, experimental results of five fuel samples (Jet A-1 serving as a reference fuel, two blends and two neat HEFA-SPKs) are discussed with respect to fuel placement, heat release and emissions. The HEFA-SPKs are produced with Neste proprietary technology called NEXBTL^{TM} from waste and residue feedstocks like used cooking oil and animal fats. Neste's current HEFA-SPK production capability is 1 Mt/a. Global potential of sustainable feedstocks suitable for HEFA processes are up to 85 million metric tons of SAF per year [2].

To the authors' knowledge, this kind of investigation has been performed for the first time in an aeroengine typical combustor set-up at typical operating conditions and with sophisticated optical diagnostics.

2. MATERIALS AND METHODS

2.1 HBK-S test rig and combustor

The tests were performed in the high-pressure combustor rig at DLR Stuttgart (HBK-S), a rig that is capable to test geometrically-scaled burners and combustors at gas turbine relevant operating conditions. The extremely good optical access to the test section enables detailed investigations of combustion phenomena by means of optical and laser diagnostics. A more detailed description of the rig can be found in [16, 17].

A two stage, rich-quench-lean RQL-type combustor was used to study the influence of various fuels on combustion performance. A sketch of the burner and combustor integrated in the HBK-S is shown in Figure 1.

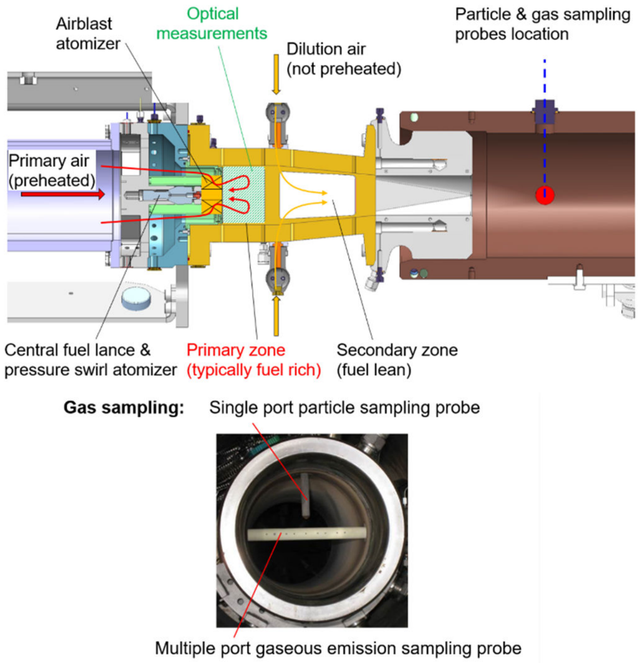

Figure 1: Sketch of the RQL-type combustor integrated in the HBK-S.

A combination of a pressure swirl and airblast atomizer, typical for aeroengines, was used in the combustor. The liquid fuel spray generated by an air-blast atomizer is fed to the combustor primary zone. The air-blast atomizer was designed by DLR and a commercial pressure swirl atomizer (Schlick, type 103, ≈ 70° spray cone) was used as a primary atomizer. The combustor primary zone had a squared cross section of 74 x 74 mm^2 and was 70 mm long. Non-preheated dilution air was added at the exit of the primary zone by two opposed rows of air injection holes. The secondary zone was 130 mm long and the top and bottom wall were convergent, resulting in a rectangular cross section of 50 x 74 mm^2 at the combustor exit. A water-cooled exhaust gas nozzle was installed to connect the combustor exit with the exhaust gas pipe.

2.2 Operating conditions and fuels tested

The combustor was operated at pressures up to p = 10 bar and at primary air preheating temperatures up to T_a = 773 K. The primary and secondary air flow rates were adapted to the operating pressure and air preheating temperature in order to keep the bulk velocity in the primary zone constant. The equivalence ratio in the primary zone Φ_{pz} was varied by the fuel flow rate keeping the primary and secondary air flow rates constant. For each fuel, the stochiometric air fuel ratio AFR_{stoich} was calculated from the hydrogen content and used for the equivalence ratio calculation. The comparison of the results for each fuel at each operating condition was performed keeping Φ_{pz} constant. In other words, the comparison was performed at approximately constant thermal power. The differences in the mass flow rate of the fuels tested, to achieve the same thermal power, were below 0.5 g/s (≈ 2 %).

The text matrix was chosen as a compromise of covering aeroengine relevant inlet temperature and pressure conditions, feasible operational range of the combustor, amount of fuel available and testing time needed. Three inlet temperatures, two pressures and a range of equivalence ratios in the primary zone both on the lean and the fuel rich side were selected (see Table 1). In order to measure particulate matter emissions which were below the detection limit at the beforementioned operating conditions, the test matrix was extended by 7.5 bar, 673 K and fuel rich conditions. The combustor was tested for a range of equivalence ratios resulting in a total thermal power P_{th} between 290 and 1091 kW. At some operating conditions, e.g. 5 bar, 673 K for all fuel samples except HEFA-A (see Table 2) and at 10 bar, 773 K for all fuel samples, measurements could also be performed at a higher equivalence ratio in the primary zone of Φ_{pz} =1.43 (see values in brackets in Table 1).

p [bar]	T$_a$ [K]	Φ$_{pz}$ [-]	Φ$_{sz}$ [-]	P$_{th}$ [kW]
5	**623, 673**	0.71 – 1.25 (1.43)	0.34 – 0.69	290 – 589
7.5	**673**	1.25 – 1.66	0.60 – 0.79	765 – 1025
10	**673, 773**	0.71 – 1.33 (1.43)	0.34 – 0.69	504 – 1091

Table 1: Operating conditions.

Five fuel samples were produced, prepared and delivered by Neste for the high-pressure measurements in the HBK-S. For establishing a baseline, one Jet A-1 reference fuel (Jet A-1) meeting the ASTM D1655 standard requirements was selected. In order to investigate the fuel composition's effect within the current blending limits, Jet A-1 was blended with HEFA-SPK type of Neste SBC (HEFA-A) in volume ratios of 30 % (Blend-30-A) and 50 % (Blend-50-A). While this HEFA-A is produced in commercial quantities, a pilot sized batch of a second HEFA-SPK (HEFA-B) was produced, targeting to evaluate the spectrum in performance and emissions within the HEFA-SPK property range. In terms of sustainability, according to the CORSIA life cycle assessment methodology [18], these kind of waste, residue and by-product feedstock based SAF GHG emission reductions are in the range of 75 - 84 % compared to the conventional jet fuel baseline.

A selection of the most important fuel properties linked to combustion and emissions behaviour are presented in Table 2. Increasing the HEFA-A content in the blends (Blend-30-A & Blend-50-A) leads to a decreased aromatic content and an increased H-content in the resulting fuel mixture. While both neat HEFA-SPKs contain virtually no aromatics, there are other notable differences in their properties: the first one being a lower density and viscosity of the HEFA-B sample. Furthermore, the HEFA-B's hydrogen content is the highest, and the surface tension is the lowest. HEFA-A has the highest viscosity and the highest derived cetane number which is a measure of fuel's reactivity. For each fuel the stoichiometric air fuel ratio AFR_{stoich} was calculated with the H-content of each fuel, resulting in the lowest value for the reference fuel Jet A-1 and the highest for HEFA-B.

	Jet A-1 Reference	Blend-30-A	Blend-50-A	HEFA-A HEFA-SPK-A	HEFA-B HEFA-SPK-B
Density [kg/m^3], ASTM D4052	799.3	791.1	785.5	771.8	757.5
Viscosity [mm^2/s], ASTM D445	1.56	1.91	2.22	3.26	1.94
Surface tension [Nm/m], ASTM D971M	24.82	24.64	24.74	24.59	23.73
Distillation temp. [K], ASTM D86	468.7	488.9	498.2	521.9	488.1
H- Content [m. %], ASTM D7171	13.92	14.28	14.53	15.17	15.30
Aromatics [vol. %], ASTM D6379	15.8	11.1	7.9	< 0.2	< 0.2
Net calorific value [MJ/kg], ASTM D4809	43.101	43.309	43.490	43.992	43.792
Cetane number [-], ASTM D6890	43.9	50.3	54.4	65.6	61.0
AFR_stoich. [-]	14.688	14.770	14.828	14.973	15.004

Table 2: Properties of the fuels tested. Density is at 288 K, viscosity at 293 K, and distillation temperature is the average of T10, T50 and T90.

2.3 Measurement techniques

Gaseous emission measurements: The NO_x (NO, NO_2) and CO emissions together with the O_2 and CO_2 exhaust gas concentrations were measured with a classical exhaust gas analysis system and a multiple port suction probe located approximately 84 mm downstream of the combustion chamber exit (see Figure 1). The NO and NO_2 concentrations were determined by means of UV absorption (ABB Limas 11), the CO and CO_2 concentrations by IR absorption (ABB URAS 26), and the O_2 concentration by paramagnetism (ABB Magnos 206) at dry conditions. The NO_x and CO concentrations measured were converted to their corresponding emission indices EI_i. The measured emission data recorded every 5 s were averaged for the time interval (> 2 min) of stable operating conditions.

Particulate measurements: The water-cooled single port sampling probe was installed 84 mm downstream of the combustion chamber exit (see Figure 1). The aerosols are fed to the sampling system via a heated sampling hose (Hillesheim, 20 m length, 8 mm inner diameter, 398 K) with a stainless steel core. The sampling system consists of a functional unit for pressure reduction to ambient conditions followed by a heated dilution system (DI-1000, Dekati, 453 K, dilution medium: N_2). A fast aerosol sizer (DMS500) from Cambustion was used to measure particles. The aerosol is pre-selected via a cyclone (1 µm), then the particles are uniformly loaded via a corona charge and afterwards sent into an electric field. Particles can be discharged at 16 different electrometer rings by separation via electromobility. The particle size distribution was recorded in the range from 5 nm to 1 µm with a data recording rate of 1 Hz. The optimum particle concentration was adjusted as required using an internal disk diluter. The aerosol measurements were supplemented by qualifying gas measurements using FT-IR (MKS, Multigas 2000). The spectrometer is operated on the sampling system and allows a comparison with the data acquisition system of the test rig.

OH* Chemiluminescence (CL) measurements: In order to gain information on the flame shape and position, the hydroxyl chemiluminescence (OH*-CL) signal was recorded. OH radicals in the electronically excited state (OH*) are formed by chemical reactions in the reaction zone, predominantly in hydrocarbon flames via the reaction $CH + O_2 \rightleftarrows CO + OH^*$ [19]. OH* is only formed within the flame front and has a short lifetime and thus provides a good qualitative heat release marker. The CL signal was imaged from the top and side using two intensified sCMOS camera units (LaVision IRO and Imager sCMOS). The intensifier / camera systems were equipped with a Halle UV quartz lens (focal length f = 64 mm; side view) and a Nikkor UV quartz lens (focal length f = 105 mm; top view) in combination with interference filters (resulting in a transmission window at 310 ± 15 nm). The resulting field of view were 80 x 175 mm^2 (side and top view) with a pixel resolution of 0.16 mm. For each operating condition, 500 single instantaneous images were recorded with a frame rate of 40 Hz with both cameras. An Abel transformation was applied to the OH*-CL images and subsequently the average determined in order to better illustrate the flame shape.

Mie scattering: The detection of Mie scattering ($\lambda \approx d_p$) of a laser sheet from droplets enables the determination of the spray penetration depth and liquid loading in the combustion chamber. It is worth pointing out that the Mie scattering signal intensity is dependent on the droplet number density and droplet size. Thus, a high signal intensity can either stem from a large number of small droplets, a few large ones, or their combination. Although these signal sources cannot be separated, a high Mie signal intensity is indicative of a high liquid fuel mass fraction.

A flashlamp-pumped Nd:YAG laser (Litron Nano L 200-15 PIV) was used (λ = 532 nm, pulse duration 5 ns) for the illumination of the spray. A set of (anti-reflective coated) cylindrical lenses and high-reflective mirrors converted the laser beam into a 150 mm wide and 1 mm thick laser sheet. The central, most homogeneous section, is guided vertically into the combustion chamber.

The scattered light was imaged with a CCD-camera (LaVision Imager Pro X), synchronized with the laser pulse via a programmable timing unit (LaVision PTU X) and controlled via DaVis v10.2 software. The camera was equipped with a standard Nikon lens (focal length 200 mm), covered with a narrow bandpass interference filter (532 ± 3 nm) that reduces the influence of broadband light sources such as the flame. The camera chip had an image resolution of 1600×1200 pixels^2. After image cropping, the resulting field of view was 72×54 mm^2 with a resolution of 22 px/mm.

A total of 300 images was recorded for all measured operation conditions to compile statistics. The Mie scattering measurements are encumbered by the harsh conditions at the high-pressure test rig such as temporal fluctuations of density, temperature and laser fluence and degrading window quality.

This presents a major challenge for a diagnostic technique based on elastic light scattering (e.g. Mie scattering or PIV) as stray light formed at the window surface cannot be spectrally filtered. In addition to regular window replacement, the instantaneous images are processed by means of a dynamic background subtraction. The background is compiled using a set of filters: (1) sliding minimum ($l_f = 100$ images) in the time domain, (2) spatial sliding maximum ($l_f = 21$ pixels) and (3) spatial sliding Gaussian ($l_f = 51$ pixels). This allows to account for stationary patterns caused by light reflections and spatially varying impurities on the windows. The laser scattering of the burner baseplate is solely dependent on the laser fluence and the window quality of the laser entry side. This reflection is subsequently used to account for temporal window quality variation and laser fluency fluctuations. It thus facilitates the comparability between cases when determining the mean and rms values of dispersed phase Mie scattering to evaluate the shape and penetration depth of the spray within the combustion chamber.

The spray penetration depth l_{pd} was determined by first integrating the average Mie scattering signal in radial direction (in the range of y = ± 15 mm) followed by a global thresholding ($\theta = 0.10$). While this method is arguably crude, it was consistently applied to all cases and offers a qualitative comparison for the different fuels and operation conditions. A sensitivity analysis is conducted with $0.075 \leq \theta \leq 0.125$ to illustrate the effect of the selected threshold on the determined penetration depth. While it inherently exhibits an effect on the determined value, the fuel trends remain valid which confirms the consistency of the procedure.

3. RESULTS AND DISCUSSION

Selected results with respect to fuel placement, spray penetration, heat release / flame zone as well as emissions measurements are discussed in this chapter. Special emphasis was put on the discussion of fuel effects and on particulate emissions at the fuel richest operating condition.

3.1 Fuel placement, spray penetration depth

In Figure 2, a map of averaged images of the liquid fuel distribution measured with Mie scattering is shown. Each image represents the signal intensity distribution in the region of x = 0 - 30 mm and y = ± 37 mm in the primary zone and is averaged over 300 single shots measured at a pressure of 10 bar, 673 K air preheating temperature and a variation of the primary zone equivalence ratio from $\Phi_{pz} = 0.71$ to 1.33. In Figure 2, some images are missing either due to difficulties during the Mie scattering measurements, e.g. for Jet A-1, $\Phi_{pz} = 0.71$ or Blend-30-A, $\Phi_{pz} = 1.0$ or due to high pressure pulsations associated with a high risk of breaking the windows (HEFA-A, $\Phi_{pz} = 0.91$, 1.00).

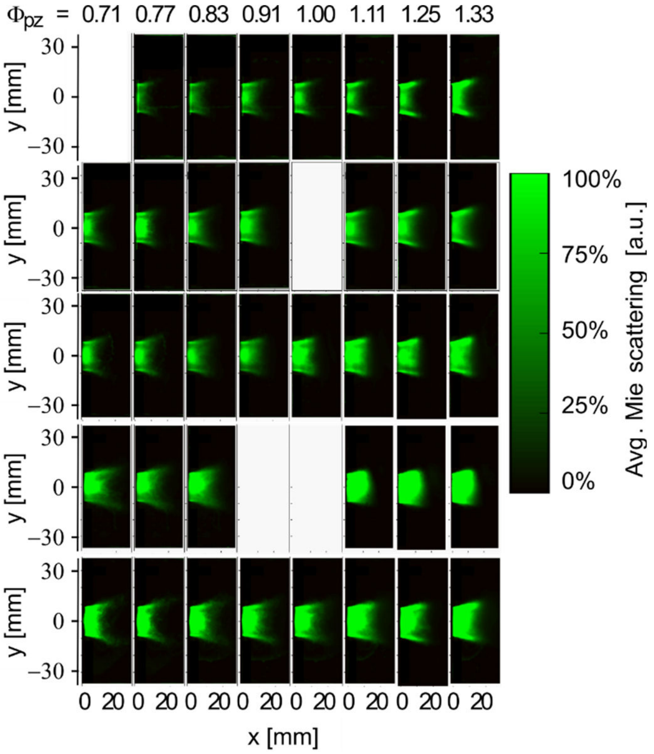

Figure 2: Averaged spray distribution at p = 10 bar, T_a = 673 K, equivalence ratios sweeps.

The Mie signal intensity and the spray penetration increase with equivalence ratio and thus liquid loading for all fuels investigated. For the reference fuel Jet A-1 and the two blends, the spray penetration is highest in the annular region downstream of the atomizer lip, whereas less fuel is found in the central near-nozzle region. This behaviour is less pronounced for the HEFA-SPK fuels (HEFA-A, HEFA-B). Particularly for the HEFA-A, significantly higher signal intensities are measured in the central near-nozzle region compared to the two blends and Jet A-1. This can be attributed to a different performance of the pressure swirl atomizer used in the injection system for fuels with a higher viscosity. It is well established that pressure swirl atomizers are susceptible to fuel viscosity, and to the difference between the fuel injection pressure and combustor operating pressure. For a higher fuel viscosity and lower pressure difference, a poor atomization has been observed (spray cone less wide, or no spray formed) [20]. For a constant operating condition, the difference between the fuel injection pressure and combustor operating pressure was for all fuels approximately the same in the present study. However, at fuel lean conditions this difference is by a factor of 4 - 5 lower than at fuel rich conditions. Therefore, at lean operation conditions for HEFA-A compared to the other fuel samples, the spray cone is presumably less wide. This results in less fuel at the airblast atomizer lip and more droplets in the central near nozzle region explaining the higher Mie signal measured in this region. As a consequence, the atomization is less perfect resulting in a higher Sauter mean diameter (SMD) and therefore higher fuel penetration of

HEFA-A in comparison with the other samples. This hypothesis of slightly higher SMD values in the case or HEFA-A are supported by a fuel assessment performed showing a 10 % increase of SMD for HEFA-A.

It should be mentioned here that the fuel injection system used in the experiments was designed for Jet A-1 and is therefore not optimised for neat HEFA-SPKs. In addition, the experiment shows that the fuel injection system operated at lean condition was for HEFA-A close to this system operational limit. For an optimal performance, fuel injection systems designed for Jet A-1 must be adapted to the different properties of SAF, particularly for lower power and low temperature conditions, e.g. idle and approach.

This can be even better illustrated by means of the spray penetration depth as shown in Figure 3 for measurements at 10 bar, 673 K and a variation of the primary zone equivalence ratio. Comparing the fuels for a constant equivalence ratio it is obvious that the spray penetration of the two HEFA-SPK fuels is higher than for all other fuel samples.

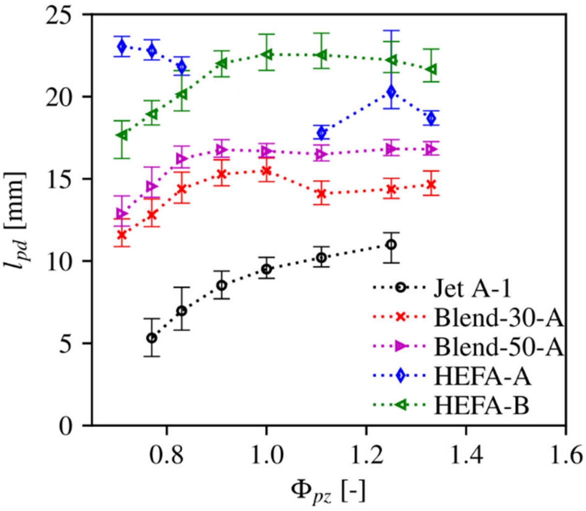

Figure 3: Spray penetration depth l_{PD} at p = 10 bar, T_a = 673 K, Φ_{pz} = 0.71 - 1.33. The markers show the values determined at $\theta = 0.10$ and the bars the threshold sensitivity.

As mentioned before, the spray penetration depth is increasing for all fuels investigated due to a higher fuel loading with increasing Φ_{pz}. In addition, a clear ranking of the fuels with respect to the spray penetration depth is visible in Figure 3. The lowest values are measured for the reference fuel Jet A-1, followed by the two blends with 30 % and 50 % HEFA-A content, and the two neat HEFAs HEFA-A and HEFA-B. This can be attributed to a different atomization and evaporation behaviour of the samples due to differences in viscosity, density and averaged distillation temperature (see Table 2). In addition, the spread between the curves is more pronounced at lean conditions. At Φ_{pz} = 0.77 a factor of ~ 4 is visible between Jet A-1 and HEFA-B whereas at Φ_{pz} = 1.25 the factor is much lower (~ 2). Thus, with increasing fuel mass flow rate and thus injection pressure, the effect of physical fuel properties is dampened, yet distinct. This is in line with the findings by Dafsari et al. [20] and Dernotte et al. [21]. A different trend is observed for HEFA-A, particularly at lean conditions (Φ_{pz} = 0.71 - 0.83), which can be explained by the different primary atomization behaviour described above.

For a higher air preheating temperature of 773 K the values of the spray penetration depth are significantly lower because of a higher fuel evaporation rate at higher temperature (see Figure *4*). At this high temperature operating condition, the measured results of all fuel samples show the same trend.

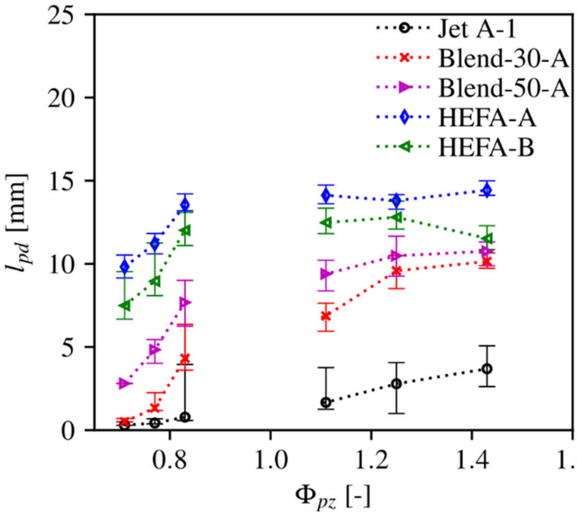

Figure 4: Spray penetration depth l_{PD} at p = 10 bar, T_a = 773 K, Φ_{pz} = 0.71 - 1.43. The markers show the values determined at $\theta = 0.10$ and the bars the threshold sensitivity.

The characteristics with respect to the fuel ranking, the spread between the curves as well as the increase of the penetration depth with increasing equivalence ratio are also observed at this air preheating temperature. The highest values of the spray penetration depth are measured for the HEFA-A fuel, which can be explained by the different atomization behaviour due to the highest viscosity of all fuels investigated (Table 2). Because of a ≈ 20 K higher fuel temperature at this operating condition of T_a = 773 K (323 K versus 303 K for T_a = 673K), a better primary atomization performance is expected with HEFA-A at lean conditions. This is in line with findings of Dafsari et al. [20], who report a less pronounced influence of viscosity changes due to different fuels used at higher fuel temperatures.

However, since the HEFA-B shows a similarly increased liquid penetration depth while still having lower viscosity than Blend-50-A and many of the physical properties similar to Blend-30-A, it is possible that at these conditions the change in behaviour is affected by properties other than solely viscosity. Another possible explanation might be linked to the difference in the fuel densities, with the reduction increasing the spray penetration depth due to the higher injection momentum for a given fuel mass flow rate.

The characteristics of the spray penetration depth rise with Φ_{pz} and the curve spread are also maintained at a pressure of 5 bars and an air preheating temperature of 623 K (see Figure 5). However, at this operating condition the values of HEFA-B are in the same range with the blends and match well with Blend-30-A. Based on this observation at this condition, sample's viscosity, density and average distillation temperature seem to correlate well with the spray penetration depth results. Unfortunately, due to high pressure pulsation amplitudes in the primary zone, measurements with HEFA-A could not be performed at these low-temperature and low-pressure conditions. Due to the lowest fuel injection pressure and fuel temperature measured at this condition, the atomization behaviour of HEFA-A was not optimal which resulted in high pressure pulsations. Although this pulsation behaviour of HEFA-A might be specific to the burner configuration used, the observation indicates that fuel injection systems designed for Jet A-1 must likely be adapted in order to achieve an optimal atomization performance when going beyond current engineering experience in terms of fuel properties.

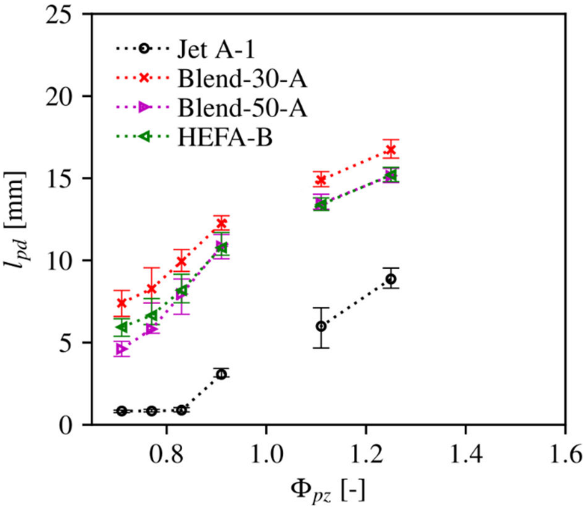

Figure 5: Spray penetration depth l_{PD} at p = 5 bar, T_a = 623 K, Φ_{pz} = 0.71 - 1.33. The markers show the values determined at $\theta = 0.10$ and the bars the threshold sensitivity.

3.2 Heat release, NO$_x$ and CO emissions

The results of the OH* chemiluminescence and the emission measurements are discussed with the help of the following figures. In Figure 6, the typical results of the heat release zone measured with OH* chemiluminescence are presented. The average of 500 Abel transformed single shot images document that a lifted v-shaped flame is formed in the primary zone. No pronounced fuel effects on the global flame features like flame lift-off height, flame position, flame angle and length were found in this investigation (see Figure 6). A similar flame angle is observed for all fuels investigated because the flame angle is dominated by the flow pattern imposed by the air blast atomizer spray cone and the swirling motion, inducing a vortex breakdown with a strong inner recirculation zone.

However, from a closer look at the OH*-CL signal distribution it is obvious that an increasingly higher OH*-CL signal is measured in the near nozzle region with increasing HEFA-A content in the fuel. The reason is a different pressure swirl atomizer behaviour when HEFA-A is used, resulting in more droplets in the near nozzle region. In the region at x = 0 mm, -8 < y < 8 mm (marked in Figure 6 with red circle) region higher OH*-CL signal is measured indicating a higher heat release in this region. The shape of the HEFA-A flame is also different due to higher fluctuations observed for this fuel. Single shot images indicate that the flame is fluctuating back and forth and a dedicated flame location, as it is the case for the other fuels, could not be observed. This observation is also supported by images of the standard deviation which show a broader signal distribution for HEFA-A.

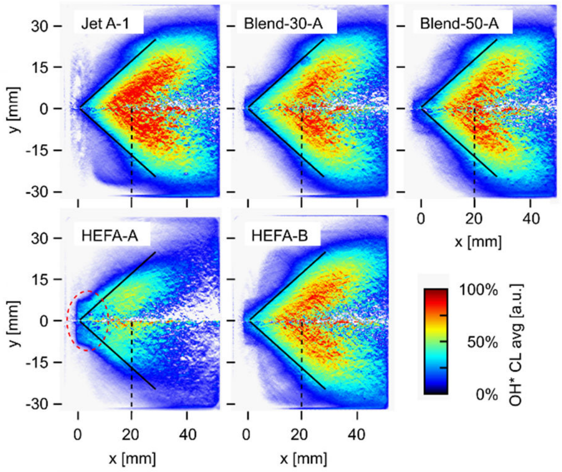

Figure 6: Fuel comparison of averaged OH*-CL images at p = 10 bar, T_a = 673 K, Φ_{pz} = 0.71. The mean flame position (maximal OH*-CL signal intensity) at the axis of symmetry (y = 0 mm) are illustrated with a black dashed line.

Typical NO$_x$ and CO emissions results are shown in Figure 7. At an air preheating temperature of 673 K, the emission index of NO$_x$ $EINO_x$ is peaking at Φ_{pz} around 1. This is expected because the dominating thermal NO formation route strongly depends on flame temperature which peaks at close-to stoichiometric conditions. The NO$_x$ emissions of the fuels investigated are very similar, and only the values of the HEFA-B fuel are slightly lower (≈ 10 %). This finding is in good agreement with the reported fuel effects on emissions reduction [9].

At a preheating temperature of 773 K, the $EINO_x$ values are higher and the gradient of the curves are steeper, which can both be explained by the exponential temperature dependence of thermal NO formation. Higher air preheating increases the flame temperature and therefore the NO$_x$ emissions. The values of HEFA-A and HEFA-B are slightly lower (≈ 14 %) than the ones for reference fuel Jet A-1. The highest NO$_x$ values were measured at this condition for Jet A-1. The values of the blends (Blend-50-A, Blend-30-A) are in the range between the reference fuel and HEFA-A, HEFA-B. In general, the measured fuel effect on NO_x reduction is in a good agreement with earlier findings [9]. Conditions with very high flame temperatures were not measured (nearly stoichiometric conditions) in order to avoid the fast window degrading associated with high temperature conditions.

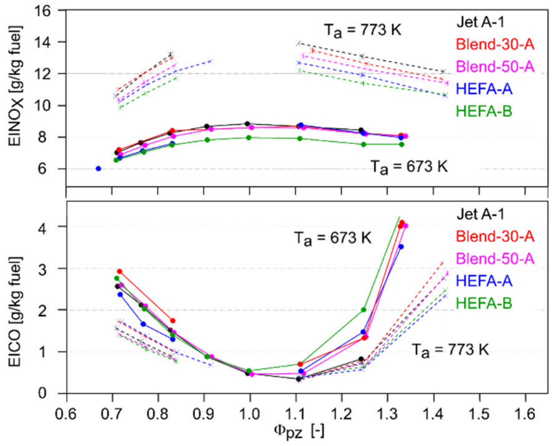

Figure 7: *$EINO_x$* (top) and *EICO* (bottom) at $p = 10$ bar, $T_a = 673$ K and 773 K, $\Phi_{pz} = 0.71$-1.33, respectively 1.43 at 773 K.

The curves of the measured emission index *EICO* show the expected trend for both air preheating temperatures. The lowest values are measured close to stoichiometric conditions and the values increase for leaner and richer conditions. The increase of the emissions on the fuel lean side can be explained by a drop of flame temperature leading to a slower and therefore incomplete CO oxidation, whereas the increase on the fuel rich side is attributed to the deficit of oxygen at fuel rich conditions which also leads to an incomplete CO oxidation. The gradient of the *EICO* increase is steeper at an air preheating temperature of 673 K because CO oxidation is very temperature sensitive. No significant fuel effect is observed at these operating conditions. This was also the case for the other investigated operating conditions not shown here.

3.3 Fuel effect on particulates at fuel richest condition

A significant fuel effect was found with respect to the particle emissions at very fuel rich conditions in the primary zone. For this reason, the results including the spray pattern are discussed in more detail for this operating condition.

In Figure 8, the characteristic results of the spray measurements with Mie scattering are shown. The scaling used in Figure 8 differs by a factor of 2.5 from the one used in Figure 2 for an improved comparison of the results for each fuel sample. The averaged images are plotted in the left column followed by a column showing the standard deviation and typical single shot images on the right-hand side in this figure. From the results of the reference fuel (Jet A-1), it is clearly visible that the spray is concentrated in the region close to the annular spray cone. Less fuel is observed in the axial near nozzle region. With increasing HEFA-A content in the fuel (Blend-30-A, Blend-50-A, HEFA-A), increasingly more fuel is found in the axial near nozzle region. The spray penetration depth is the largest for HEFA-A. As discuss earlier, this difference of the spray characteristics can be attributed to the fuel properties of HEFA-A (see Table 2) resulting in a different fuel atomization and therefore different liquid fuel distribution.

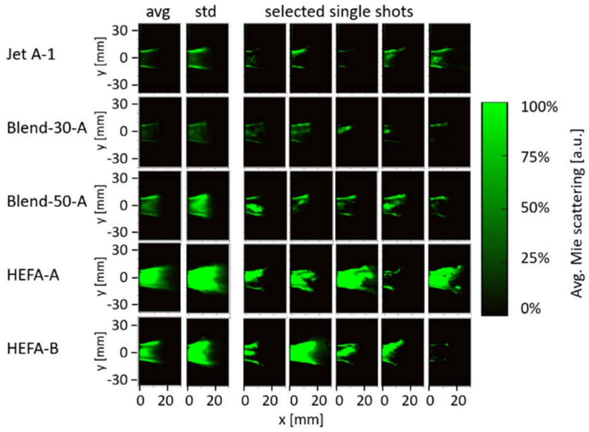

Figure 8: Spray characteristics (averaged (avg), standard deviation (std) images, selection of single shots) at $p = 7.5$ bar, $T_a = 673$ K, $\Phi_{pz} = 1.66$. For a better illustration, a scaling different from Figure 2 is used here.

Comparing the average distillation temperatures of the fuels (Table 2), HEFA-A has the highest value indicating a lower evaporation rate compared to the other fuels. Although different spray characteristics were found for the fuels investigated, the same or very similar behaviour was observed with respect to heat release, flame shape and gaseous emission characteristics at this operating condition.

However, a significant fuel effect on particulates was derived at the fuel richest operating condition. At other operating conditions the measured particulate matter emissions were extremely low, mainly below the detection limit. The results of the particle measurements are presented in the Figure 9-11. The particle size distribution of each fuel is shown in Figure 9.

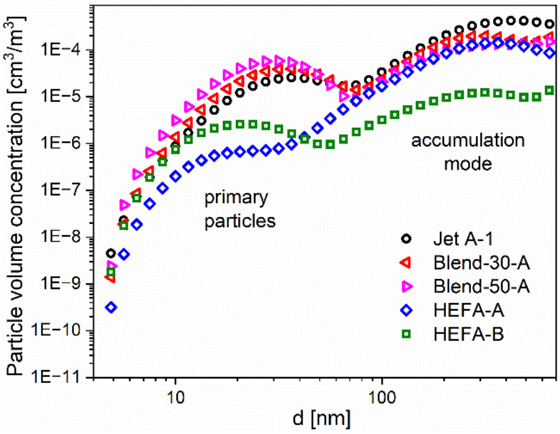

Figure 9: Particle size distributions at $p = 7.5$ bar, $T_a = 673$ K, $\Phi_{pz} = 1.66$.

Variations in the primary particle sizes were measured for the different fuels. The two HEFA-SPK fuels (HEFA-A, HEFA-B) showed narrow primary particle modes in contrast to the reference fuel (Jet A-1) and the two blends (Blend-50-A, Blend-30-A). From this plot, it is obvious that in addition to the primary particles also an accumulation mode at $d_p > 100$ nm is visible in the measured particle size distributions. The particle volume concentration is dominated by the accumulation mode particles due to the d_p^3 dependence, with HEFA-B featuring the lowest values in both modes as shown in Figure 9. The lowest concentration of primary particles was measured for HEFA-A.

A clear ranking of the fuels with respect to the integrated particle volume was observed (see Figure 10). The highest value was measured for the reference fuel (Jet A-1) followed by the two blends (Blend-30-A, Blend-50-A) and the two neat HEFAs (HEFA-A, HEFA-B). The lowest integrated particle volume was measured for HEFA-B.

The effect of fuel hydrogen content on relative integrated particle volume (soot reduction potential) is presented in Figure 11. The particle volume at the selected operating condition follows the expected trend with fuel H-content: the higher the H-content of the fuel, the lower the relative integrated particle volume. Overall, the lowest particle emission was measured for HEFA-B.

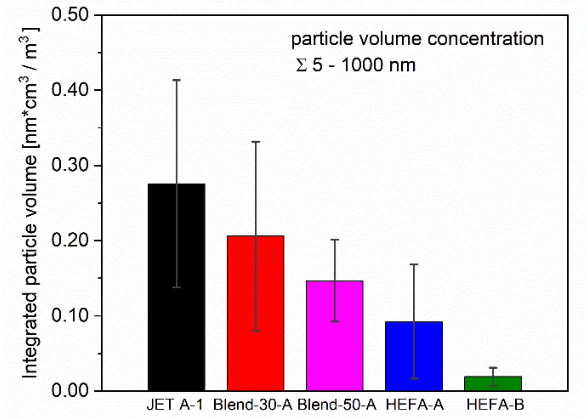

Figure 10: Integrated particle volume at $p = 7.5$ bar, $T_a = 673$ K, $\Phi_{pz} = 1.66$.

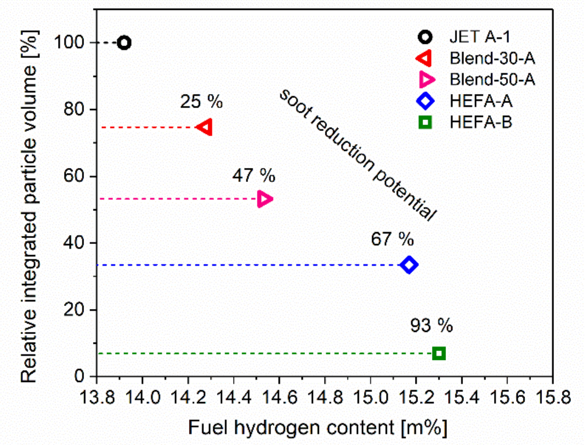

Figure 11: Relative integrated particle volume as a function of fuel H-content at $p = 7.5$ bar, $T_a = 673$ K, $\Phi_{pz} = 1.66$.

A particle emission reduction of 93 % compared to the reference fuel Jet A-1 was measured for HEFA-B and in addition, also for HEFA-A a significant reduction of 67 % was found. This is a promising result because besides HEFA-SPK's high GHG reduction potential in life-cycle perspective, it also documents its potential to lower the non-CO_2 impact of aviation.

4. CONCLUSION

Considering the future aeroengine development and optimization in order to fully unlock SAF's benefits, this study showed important insights from the combustor performance perspective.

Differences of the spray characteristics were investigated for five fuels at three different operating conditions. A higher fuel concentration (higher Mie scattering signal intensity) in the axial near nozzle region and elevated spray penetration depths were observed for both the HEFA-SPK fuels at most of the investigated conditions. The findings of this study indicate that for an optimal combined performance beyond the currently allowed 50 % SAF blends, the fuel injection system designed for Jet A-1 must be adapted to the different properties of neat SAFs. The redesign of fuel injection system could unlock additional non-CO_2 emission saving potential, as demonstrated with further reduction of soot emissions with 100 % HEFA-SPK.

Despite these observed differences in the spray penetration, no significant differences were found between the samples with respect to heat release / flame shape and gaseous emission characteristics. Furthermore, while the combustion behaviour in terms of heat release and gaseous emission characteristics was similar, a strong fuel effect was found at the fuel richest operating condition for particulate emissions. The measured particle volume concentration is dominated by the accumulation mode particles, while HEFA-B features the lowest values in both modes. A low primary particle volume concentration was measured also for HEFA-A. The reduction of the relative integrated particle volume follows the expected trend with fuel H-content and the increasing HEFA-SPK content. Overall, HEFA-B showed the lowest particle emission leading to a reduction of 93 % compared to Jet A-1 while the effect of HEFA-A blends leads to significant reductions of 25 % (Blend-30-A) and 47 % (Blend-50-A), and into 67 % reduction with neat HEFA-A.

While SAF is already identified as a major solution for decarbonizing aviation through the fuel's reduced GHG emissions over the life-cycle, this study demonstrated that HEFA-SPK type SAFs exhibit further potential in terms of reduced non-CO_2 impact through the reduction in particle emissions, and topics that should be further investigated when optimizing future engines for the use of SAF.

ACKNOWLEDGEMENTS

The authors thank the HBK-S test crew as well as the mechanics for their permanent and very important support during the preparation phase and the measuring campaign.

Fabian Hampp acknowledges the funding by the Deutsche Forschungsgemeinschaft (DFG, German Research Foundation) - project number: 456687251.

REFERENCES

[1] Waypoint 2050, Air Transport Action Group /ATG) report, Sept. 2012, https://aviationbenefits.org/media/167417/w2050_v2021_27sept_full.pdf

[2] Clean skies for tomorrow, sustainable aviation fuels as a pathway to net-zero aviation, World Economic Forum (WEF) insight report, Nov. 2020, https://www.mckinsey.com/~/media/mckinsey/industries/travel%20transport%20and%20logistics/our%20insights/scaling%20sustainable%20aviation%20fuel%20today%20for%20clean%20skies%20tomorrow/clean-skies-for-tomorrow.pdf

[3] EI 1533 Report, Quality assurance requirements for semi-synthetic jet fuel and synthetic blending components (SBC), Energy Institute, Nov. 2022, https://publishing.energyinst.org/topics/aviation/aviation-fuel-handling/ei-1533-quality-assurance-requirements-for-semi-synthetic-jet-fuel-and-synthetic-blending-components-sbc

[4] Carbon Offsetting and Reduction Scheme for International Aviation (CORSIA), International Civil Aviation Organization (ICAO), https://www.icao.int/environmental-protection/CORSIA/pages/default.aspx

[5] Renewable Energy Directive, European Union, https://energy.ec.europa.eu/topics/renewable-energy/renewable-energy-directive-targets-and-rules/renewable-energy-directive_en

[6] Standard Specification for Aviation Turbine Fuel Containing Synthesized Hydrocarbons ASTM D7566-23b, Nov. 2023, http://www.astm.org/d7566-23b.html

[7] Standard Specification for Aviation Turbine Fuels, ASTM D1655, Nov. 2022, https://www.astm.org/d1655-22.html

[8] Ministry of Defence, Defence Standard 91-091, Issue 16, 14 December 2023, https://www.jig.org/documents/defstan-91-091-issue-16/

[9] Blakey, S. L. Rye, L., Wilson, C. W., 2011, "Aviation gas turbine alternative fuels: A review", Proceedings of the Combustion Institute, **33**, pp.2863-2885, https://doi.org/10.1016/j.proci.2010.09.011

[10] Undavalli, V., Hamilton, J., Ubogu, E., Ahmed, I., Khandelwal, B., 2012, "Impact of HEFA fuel properties on gaseous emissions and smoke number in a gas turbine engine", ASME Paper No. GT2022-82201.

[11] Schripp, T., Anderson, B. E., Bauder, U., Rauch, B., Corbin, J. C., Smallwood, G. J., Lobo, P., Crosbie, E. C., Shook, M. A., Miake-Lye, R. C., Yu, Z., Freedman, A., Whitefield, P. D., Robinson C. E., Achterberg, S. L., Köhler, M., Oßwald, P., Grein, T., Sauer, D., Voigt, C., Schlager, H., LeClerc, P., 2022, "Aircraft engine particulate matter emissions from sustainable aviation fuels: Results from ground-based measurements during the NASA/DLR campaign ECLIF2/ND-MAX", Fuels, **325**, 124764, https://doi.org/10.1016/j.fuel.2022.124764

[12] Märkl, R. S., Voigt, C., Sauer, D., Dischl, R. K., Kaufmann, S., Harlaß, T., Hahn, V., Roiger, A., Weiß-Rehm, C., Burkhardt, U., Schumann, U., Marsing, A., Scheibe, M., Dörnbrack, A., Renard, C., Gauthier, M., Swann, P., Madden, P., Luff, D., Sallinen, R., Schripp, T., and Le Clercq, P., 2024, "Powering aircraft with 100 % sustainable aviation fuel reduces ice crystals in contrails", Atmospheric Chemistry and Physics, **24**, pp. 3813–3837, https://doi.org/10.5194/acp-24-3813-2024.

[13] Khandelwal, B. Cronly, J., Ahmed, I.S., Wijesinghe, C.J., Lewis, C., 2019, "The effect of alternative fuels on gaseous and particulate matter (PM) emission performance in an APU", The Aeronautical Journal, **123**, pp. 617-634, https://doi.org/10.1017/aer.2019.16

[14] Buffi, M., Valera-Medina, A., Marsh, R., Pugh, D., Giles, A., Runyon, J., Chiaramonti, D., 2017, "Emissions characterisation tests for hydrotreated renewable jet fuel from used cooking oil and its blends", Applied Energy, **201**, pp. 84-93, https://doi.org/10.1016/j.apenergy.2017.05.104

[15] Harlass, T., Dischl, R., Kaufmann, S., Märkl, R., Sauer, D., Scheibe, M., Stock, P., Bräuer, T., Dörnbrack, A., Roiger, A., Schlager, H., Schumann, U., Schripp, T., Grein, T., Bondorf, L., Renard, C., Gauthier, M., Johnson, M., Luff, D., Madden, P., Swann, P., Ahrens, D., Sallinen, R., and Voigt, C., 2024,

"Measurement report: In-flight and ground-based measurements of nitrogen oxide emissions from latest generation jet engines and 100% sustainable aviation fuel", EGUsphere [preprint], https://doi.org/10.5194/egusphere-2024-454

[16] Fleck, J., Griebel, P., Steinberg, A., Stöhr, M., Aigner, M., Ciani, A., 2010, "Experimental investigation of a generic, fuel flexible reheat combustor at gas turbine relevant operating conditions," ASME Paper No.GT2010- 22722.

[17] Rödiger, T., Lammel, O., Aigner, M., Beck, C., Krebs, W., 2013, "Part-load operation of a piloted FLOX® combustion system", J. Eng. Gas Turbines Power **135** (3), 031503, https://doi.org/10.1115/1.4007754

[18] CORSIA supporting document, https://www.icao.int/environmental-protection/CORSIA/Documents/CORSIA_Eligible_Fuels/CORSIA_Supporting_Document_CORSIA%20Eligible%20Fuels_LCA_Methodology_V5.pdf

[19] Hardalupas, Y., Panoutsos, C. S., Taylor, A. M. K. P., 2010, "Spatial resolution of a chemiluminescence sensor for local heat-release rate and equivalence ratio measurements in a model gas turbine combustor", J. Exp. Fluids, **49**, 883-909, https://doi.org/10.1007/s00348-010-0915-z

[20] Dafsari, R. A., Lee, H. J., Han, J., Lee, J., 2019, "Evaluation of the atomization characteristics of aviation fuels with different viscosities using a pressure swirl atomizer", J. of Heat and Mass Transfer, **145**, 118704, https://doi.org/10.1016/j.ijheatmasstransfer.2019.118704

[21] Dernotte, J., Hespel, C., Foucher, F., Houillé, S., Mounaïm-Rousselle, C., 2012, "Influence of physical fuel properties on the injection rate in a Diesel injector", Fuel, **96**, pp. 153-160, https://doi.org/10.1016/j.fuel.2011.11.073